Synthetic Metals 160 (2010) 2028–2036

Contents lists available at ScienceDirect

Synthetic Metals

journal homepage: www.elsevier.com/locate/synmet

Covalent functionalization of graphene oxide with polyglycerol and their use as templates for anchoring magnetic nanoparticles

Tuan Anh Pham, Nanjundan Ashok Kumar, Yeon Tae Jeong*

Department of Image Science and Engineering, Pukyong National University, Busan 608-739, Republic of Korea

ARTICLE INFO

Article history:
Received 14 June 2010
Received in revised form 14 July 2010
Accepted 22 July 2010
Available online 19 August 2010

Keywords:
Polyglycerol
Graphene
Covalent functionalization
Magnetic nanoparticles
Hybrid nanostructure

ABSTRACT

An efficient strategy for the preparation of water-dispersible hybrid material containing graphene oxide and polyglycerol for the first time is demonstrated. Pristine graphite was firstly oxidized to obtain graphene oxide with hydroxyl functional groups. Then, the covalent grafting of polyglycerol onto the surface of graphene oxide was carried out based on *in situ* ring-opening polymerization of glycidol. For the construction of novel hybrid nanostructure, Fe-core/Au-shell nanoparticles were prepared and further functionalized using 4-mercaptophenylboronic acid through the well-developed Au–S chemistry. Subsequently, magnetic nanoparticles were anchored on the surface of polyglycerol-grafted graphene nanosheets via boroester bonds. The resulting hybrid materials were characterized using a range of analytical techniques. Fourier transform infrared spectroscopy (FT-IR) was employed to investigate the initial changes in surface functionalities. While X-ray diffraction (XRD) was used to confirm the structure of graphene oxide nanosheets, high resolution transmission electron microscopy (HR-TEM), and field emission scanning electronic microscopy (FE-SEM) equipped with an energy dispersive X-ray (EDX) spectrometer were used to study the morphologies and distribution of magnetic nanoparticles onto the surface of polyglycerol-grafted graphene. Thermogravimetric analysis (TGA) was used to study the weight loss of the samples on heating. Superconducting quantum interference device magnetometer (SQUID) was employed to the magnetic property of magnetic nanoparticles. The digital images provided a vivid observation on the high dispersion stability of the prepared novel hybrid materials in distilled water.

1. Introduction

The continuous progress of nanotechnology in material science has opened new pathways for developing of novel functional materials. Among them, graphene, a flat monolayer of hexagonally arrayed sp^2-bonded carbon atoms tightly packed into a two-dimensional (2D) honeycomb lattice, has been emerging as a fascinating material due to the unique physical, chemical, electrical and mechanical properties [1–6]. In parallel with developments from the basic science perspective [7–10], graphene-based hybrid materials with the combination of its excellent properties and inexpensive sources (from either natural or synthetic sources) have attracted a great deal of attention as promising candidates for a wide variety of potential applications in catalyst supports [11,12], chemical sensors [13–16], electronic components [17–22], Li ion batteries [23,24] and even applications in biotechnology [25,26]. Among known studies for developing the graphene-based materials, utilization of graphene oxide (GO) is the most versatile and easily scalable [27]. Therefore, GO is often used as the starting material for the preparation of graphene-based hybrid materials. Although GO can be easily exfoliated into monolayer sheets in water, it is not quite ready for its potential applications due to the strong tendency of the monolayeric graphene sheet to form irreversible agglomerates into multilayeric graphite through strong π–π stacking and van der Waals interaction [28]. Therefore, the aggregation of graphene sheets poses a practical challenge, that must be addressed to expand graphene's application scope in various potential fields of nanotechnology because most of their unique properties are only associated with few layers or individual sheets of this two-dimensional hexagonally packed carbon lattice. It is well-known that the presence of covalently attached oxygen-containing groups in GO such as hydroxyl, epoxy groups on the basal plane and carboxyl groups at the edge provides a handle for further surface chemical functionalizations via well-developed carbon chemistry. Hence, several chemical methods have been explored to obtain water-dispersible graphene that include non-covalent functionalization [29,30] and covalent functionalization strategies [31–33].

Recently, a novel class of functional nanostructures has been developed to obtain the optical, electrical and catalytic properties via decorating graphene sheets with novel metal nanoparticles [34–36]. The dispersion of metal nanoparticles on graphene sheets

* Corresponding author. Tel.: +82 51 629 6411; fax: +82 51 629 6408.
E-mail address: ytjeong@pknu.ac.kr (Y.T. Jeong).

0379-6779/$ – see front matter © 2010 Elsevier B.V. All rights reserved.
doi:10.1016/j.synthmet.2010.07.034

provides new opportunities for researchers in designing novel hybrid nanostructures for various potential applications. It is well known that many types of metals can be deposited onto surface of graphene sheets. Among such nanoparticles, magnetic nanoparticles have attracted a tremendous amount of attention in recent years due to their remarkable properties and potential applications [37–40]. However, reports on the immobilization of magnetic nanoparticles on the surface of GO sheets are relatively rare. Moreover, the lack of dispersibility of magnetic nanoparticles in solvents and the irreversible agglomerates of graphene have always been major technical barriers for the construction of hybrid nanostructures containing graphene and magnetic nanoparticles.

On the basis of these observations, in this contribution, we have explored a strategy for the covalent functionalization of graphene nanosheets with a class of hyperbranched polymers (aliphatic polyether polyols) named polyglycerol (PG) and their use as templates for further loading functionalized Fe-core/Au-shell nanoparticles (Fe@Au nanoparticles) for the first time. As a result, the combination of PG and GO leads to hybrid nanostructures with high dispersibility in aqueous media mainly due to the high hydrophilicity of PG. Furthermore, the chemical grafting of PG onto the surface of GO also provides a suitable surface for their immobilization with functionalized magnetic nanoparticles to obtain novel nanostructures containing graphene, polymer and magnetic nanoparticles. To the best of our knowledge, there have been no reports available on using PG for the preparation of water-dispersible graphene hybrid nanostructures and their use as templates for loading Fe@Au nanoparticles.

In our strategy, GO was synthesized by the modified Hummer's and Offeman's method [41]. Subsequently, the chemical grafting of PG onto the GO sheets was carried out by the "grafting from" approach based on *in situ* ring-opening polymerization of glycidol [42]. Furthermore, the Fe@Au nanoparticles were synthesized using the inverse micelle method [43]. To immobilize Fe@Au nanoparticles to the PG-grafted GO (PG-*g*-GO), the surface of Fe@Au nanoparticles was functionalized by boronic acid via the well-developed Au–S chemistry. The immobilization of boronic acid-modified magnetic nanoparticles on the PG-*g*-GO obtained through boroester bonds, which was formed between hydroxyl groups of boronic acid and PG. The combination of magnetic nanoparticles and biocompatible polymer, polyglycerol on to the GO sheets surface makes us believe that the novel hybrid materials developed in this study have potential for a wide variety of applications from electromagnetic devices to novel drug delivery systems.

2. Experimental

2.1. Materials

Graphite powder from Sigma–Aldrich was used to prepare GO. Glycidol, potassium methoxide, 4-mercaptophenylboronic acid, ferrous sulfate, hydrogen tetrachloroaurate (gold solution; 30 wt.% in dilute HCl), sodium borohydride, cetyltrimethylammonium bromide, 1-butanol, octane and other chemicals were purchased from Sigma–Aldrich and used as received.

2.2. Synthesis

2.2.1. Preparation of GO

In a typical reaction, 3 g of graphite powder was added to 300 mL of cooled (0 °C) H_2SO_4. Then, 20 g of $KMnO_4$ and 3 g of $NaNO_3$ were added slowly while stirring. The temperature of the mixture was maintained below 10 °C. The mixture was then transferred to a 35 °C water bath and stirred for 30 min. Subsequently, 200 mL of deionized water was added and the temperature was increased to 98 °C and the mixture was maintained at that temperature for 30 min. The reaction was terminated by adding 500 mL of deionized water followed by the addition of 40 mL of 30% H_2O_2 solution. The color of the mixture changed to brilliant yellow, indicating the oxidation of pristine graphite to GO. The solid product was then separated by using membrane filter system, washed repeatedly with distilled water until the pH was 7 and dried at 50 °C for 24 h under vacuum.

2.2.2. Synthesis of PG-g-GO

One hundred mg of GO was mixed with saturated solution of potassium methoxide in 2 mL of methanol for 1 h in an ultrasonic bath and stirred at room temperature for 2 h. Then, the mixture was refluxed at 80 °C for 6 h and washed repeatedly with methanol. The solvent was removed by reduced pressure distillation in rotavapour. Then, 7 mL of glycidol was added to the GO and mixture was stirred for 4 h at 100 °C under nitrogen atmosphere. The mixture was cooled and dissolved in methanol. Finally, the product was precipitated in acetone and then separated by using membrane filter system.

2.2.3. Synthesis of boronic acid functionalized Fe@Au nanoparticles (B-f-MNPs)

Fe@Au nanoparticles were synthesized by a reverse micelle reaction under nitrogen atmosphere. All reverse micelle solutions were prepared using cetyltrimethylammonium (CTAB) as the surfactant, octane as the oil phase, 1-butanol as the cosurfactant, and aqueous reactant as the water phase. Firstly, 0.36 g of $FeSO_4$ in the inverse micelle solution was mixed up with 0.18 g of $NaBH_4$ in other reverse micelle solution. The mixture was stirred at room temperature under nitrogen atmosphere. The change in color of the solution from green to black, indicate the formation of Fe nanoparticles. After c.a. 1 h, 0.54 g of $HAuCl_4$ prepared as a micelle solution was added to the solution of $FeSO_4$ and $NaBH_4$. Then, 0.22 g of $NaBH_4$ in other micelle solution was immediately added to the solution. The new solution was left stirring at room temperature for 12 h under nitrogen atmosphere. The micelles in the reaction mixture were disrupted with acetone causing nanoparticles to precipitate. The dark solid was separated using a magnet and repeatedly washed with a 1:1 chloroform/methanol mixture to remove any nonmagnetic particles and organic surfactant if any. The product was then dried in vacuum oven for overnight, resulting in a black powder.

In the next step, 0.058 g of 4-mercaptophenylboronic acid was mixed with 0.03 g of Fe@Au nanoparticles in 50 mL of ethanol. After vigorous stirring for 12 h, the solvent was removed by distillation under decreased pressure. The dark residue was washed thoroughly with diethyl ether to remove excess 4-mercaptophenylboronic acid. Finally, the material was dried to obtain the pure product as a dark-brown solid.

2.2.4. Synthesis of magnetic nanoparticle-immobilized PG-g-GO (MNPs-i-PG-g-GO)

Twenty mg of PG-*g*-GO in 20 mL of ethanol were sonicated to obtain a homogeneous dispersion. Then the suspension of 0.01 g of B-*f*-MNPs in 10 mL of ethanol was added to the solution. The homogeneous black mixture was stirred at room temperature for 2 h. The resultant black mixture was filtered, washed with ethanol and distilled water using PTFE filter membrane. The black solid was dried at 40 °C in a vacuum oven.

2.2.5. Characterization techniques

HR-TEM images were recorded using Joel JEM 2010 instrument (Japan) with an accelerating voltage of 200 kV to observe the nanoscale structures, by placing a drop of the samples dispersed in distilled water on copper grids and drying. The morphology and

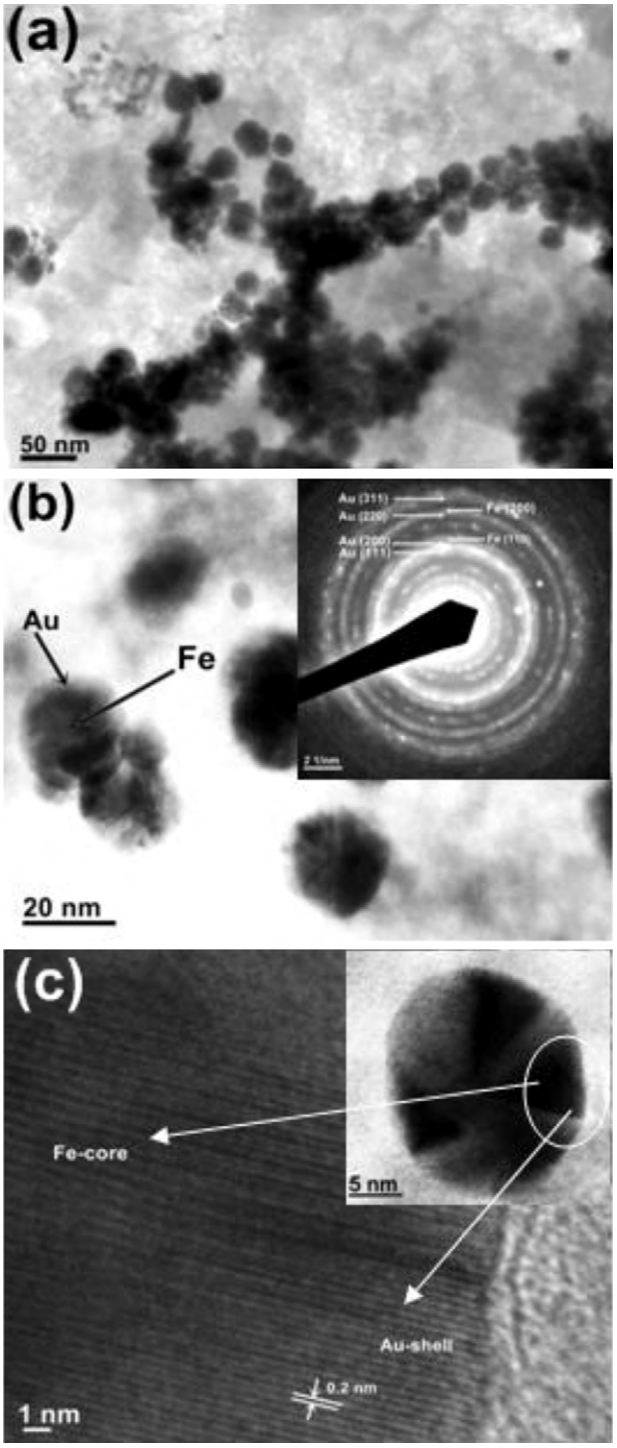

Fig. 1. (a) and (b) HR-TEM images of Fe@Au nanoparticles at different magnifications, the inset image shows diffraction pattern of a single Fe@Au nanoparticle and (c) HR-TEM image of a single Fe@Au nanoparticle.

elemental analysis of the hybrids were carried out by using FE-SEM images equipped with an EDX spectrometer (Hitachi JEOL-JSM-6700F system, Japan). The changes in the surface chemical bondings of functionalized Fe@Au nanoparticles and hybrid nanostructures were recorded by FT-IR (Perkin-Elmer Spectrum GX, USA), in the frequency range of 4000–500 cm^{-1}. Thermogravimetric analysis (TGA) was conducted with Perkin-Elmer Pyris 1 analyzer (USA). Before the test, all the samples were carefully grounded to fine powder. The samples were scanned within the temperature range

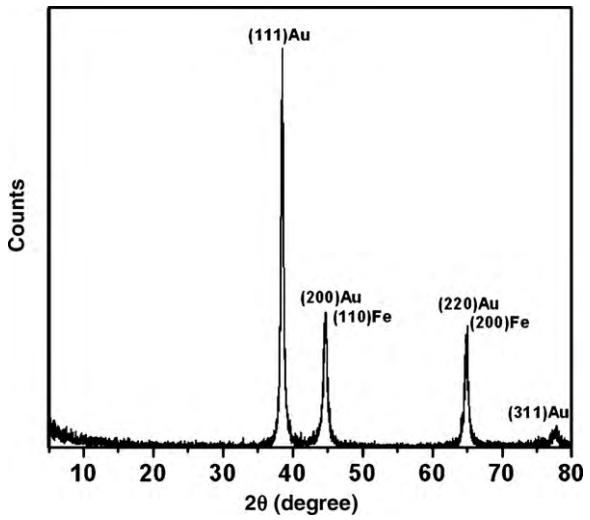

Fig. 2. XRD pattern of Fe@Au nanoparticle.

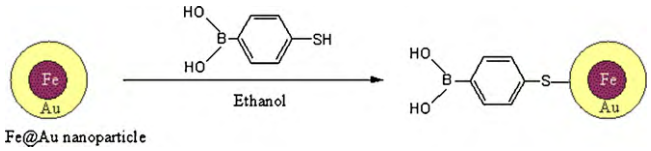

Scheme 1. Schematic illustration on the preparation of B-*f*-MNPs.

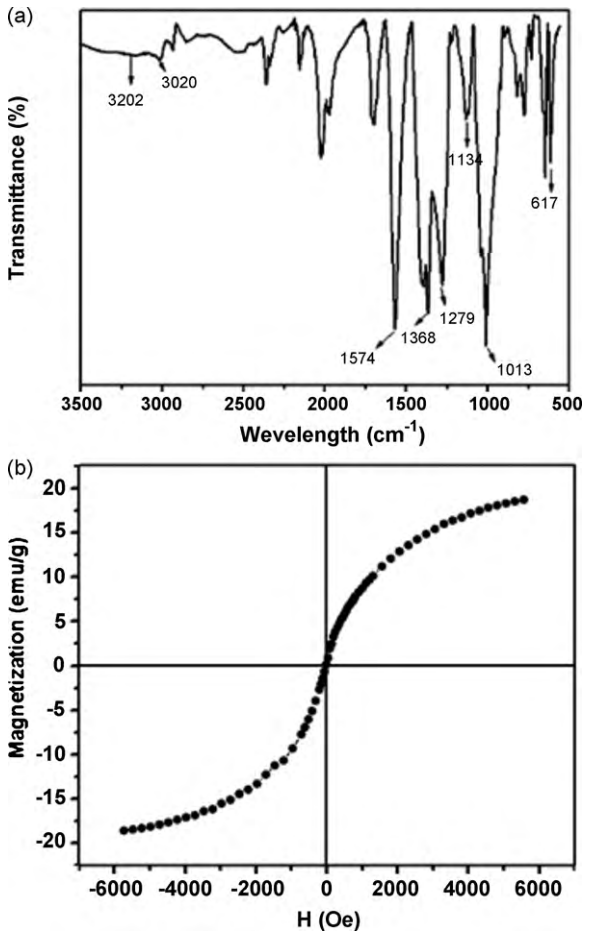

Fig. 3. (a) FT-IR spectrum of B-*f*-MNPs and (b) magnetization curves of B-*f*-MNPs.

50–700 °C at a heating rate of 10 °C min^{-1} under continuous N_2 flow. Surface composition was investigated using X-ray photoelectron spectroscopy (Thermo VG Multilab 2000) in ultra high vacuum with Al Kα. The crystallographic states of Fe@Au nanoparticles, pristine graphite and hybrids were determined by a Philips X'pert-MPD system diffractometer (Netherland) with Cu Kα radiation. Magnetic measurement was performed at 300 K using a superconducting quantum interference device magnetometer (Quantum design MPMS-XL7, USA).

3. Results and discussion

3.1. Characterization of B-f-MNPs

Fig. 1 shows HR-TEM images of Fe@Au nanoparticles. As seen from Fig. 1a, it is interesting to note that the Fe@Au nanoparticles tend to aggregate into clusters, which is a result of the coating of Au layers to Fe nanoparticles. Clear observations on the core-shell structure of Fe@Au nanoparticles were obtained using the higher magnification HR-TEM as represented in Fig. 1b. The size of Fe-core is about 16 nm while the coating of Au-shell is about 3–5 nm. The Fe-core and Au-shell are shown clearly marked arrows. In most of Fe@Au nanoparticles, shell of Au can be easily seen as bright regions in outer layer of nanoparticles, while the core of Fe appears as dark regions in the center of nanoparticles. It could be explained that Au, as a heavy element, scatters electrons more strongly than Fe with a smaller atomic number. Consequently, the brighter regions within the nanoparticles are Au rich, while the darker regions are Fe rich and Au poor [44]. The inset graph in Fig. 1b shows diffraction studies of Fe@Au nanoparticle. The presence of both Au and Fe in a single particle was indicated through the overlapping of 2 0 0 and 2 2 0 of *fcc* structured Au with 1 1 0 and 2 0 0 of *bcc* structured Fe. In addition, the lattice fringes in the Au-shells are clearly observed via high magnification HR-TEM image as seen in Fig. 1c. Their interfringe spacing is 0.2 nm, indicating the interplane distance of the (2 0 0) planes of the *fcc* Au.

More evidence, the crystalline structure of Fe@Au nanoparticles was obtained using XRD spectrum. As labeled in Fig. 2, the peaks at 38.14°, 44.36°, and 64.58° are assigned to *fcc* bulk Au of (1 1 1), (2 0 0), (2 2 0) (JCPDS 04-784). The pattern of Fe (JCPDS 06-696) is covered under the pattern of Au due to the overlapping of their diffraction peaks at 44.36° and 64.58°, indicating the presence of both Fe and Au nanoparticles in the sample.

The procedure for preparing of B-*f*-MNPs is presented in Scheme 1. To examine the surface functionalization of Fe@Au nanoparticles with boronic acid, FT-IR spectra of B-*f*-MNPs are shown in Fig. 3a. The peaks at 3020, 1574, and 1013 cm^{-1} could be assigned to the presence of aromatic ring, while aryl-boroxines typically display at a band of 1368 cm^{-1} [45]. Furthermore, the board band at 3212 cm^{-1} indicates the presence of free hydroxyl functional groups of boronic acid on the sample surface. These results confirmed that surface of Fe@Au nanoparticles were successfully functionalized with 4-mercaptophenylboronic acid.

On the other hand, to determine the magnetic property of synthesized B-*f*-MNPs, the magnetization measurement was carried out at room temperature. The saturation magnetization of the sample is 18 emu/g, indicating characteristic of superparamagnetic at room temperature presented in Fig. 3b.

3.2. Characterization of hybrid nanostructures

The schematic for preparing hybrid nanostructures is illustrated in Scheme 2. The three-step process includes: (1) the preparation of GO using Hummers and Offeman's method, (2) the chemical grafting of PG on the GO surface based on *in situ* ring-opening polymerization of glycidol and (3) the covalent immobilization of B-*f*-MNPs on the surface of PG-*g*-GO via boroester bonds. Fig. 4 shows the FT-IR results of the pristine graphite and hybrid nanostructures

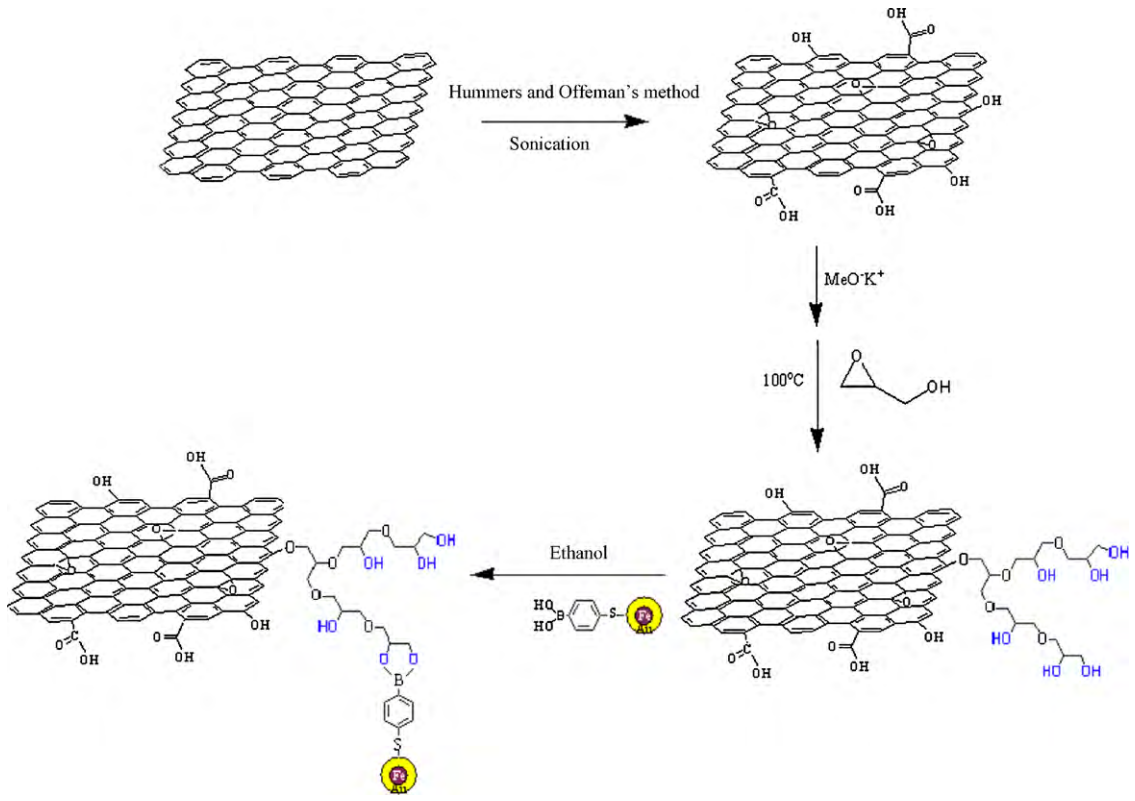

Scheme 2. Synthetic route of water-dispersible PG-*g*-GO nanostructure and its immobilization with B-*f*-MNPs.

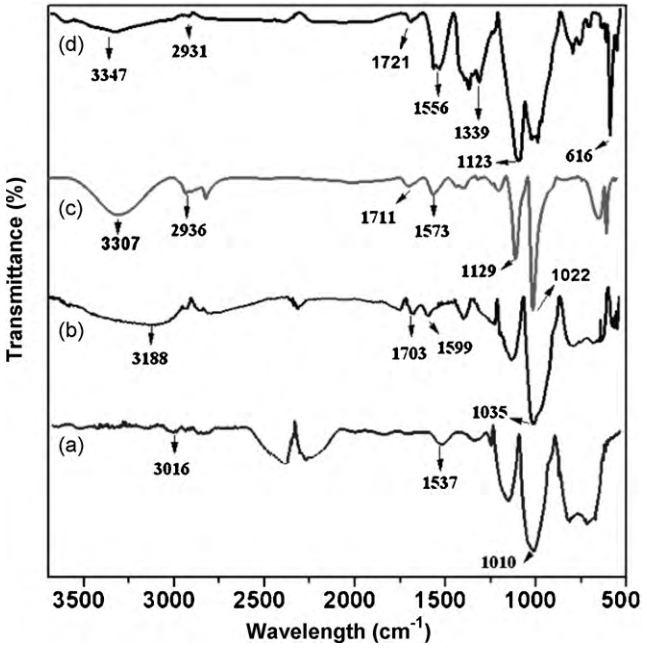

Fig. 4. FT-IR spectra of (a) pristine graphite, (b) GO, (c) PG-*g*-GO and (d) MNPs-*i*-PG-*g*-GO.

obtained at different processing step. For the pristine graphite, the peaks at 3016 and 1537 cm^{-1} are attributed to the presence of aromatic ring as shown in Fig. 4a. The FI-IR spectrum of GO differs from that of pristine graphite as evidenced by the presence of new bands at 3188 and 1703 cm^{-1}. As can be seen from Fig. 4b, the broad band at 3188 cm^{-1} could be assigned to stretching of the –OH groups on the GO surface, while the band at 1703 cm^{-1} is associated with stretching of the C=O bond of carboxylic groups. In the case of PG-*g*-GO, as seen in Fig. 4c, the peaks at around 1711 and 1573 cm^{-1} continue to be observed in apart from the all features of the GO. However, the relative increase in the intensity of the broad band at around 3307 cm^{-1} suggests that there could be more –OH groups on the surface of GO due to the presence of PG after the covalent grafting of PG to the GO surface. On the other hand, after the covalent immobilization of B-*f*-MNPs on the surface of PG-*g*-GO, significant changes were observed in the IR spectrum as shown in Fig. 4d. New peaks at 1339 and 616 cm^{-1} are assigned to B–O stretching band and B–O banding band, respectively and are clearly visible [46]. Moreover, the decrease in the intensity of the broad band around 3347 cm^{-1} was observed, indicating the density of hydroxyl groups on the PG-*g*-GO surface decreased after their reaction with boronic acid. These observations clearly confirmed the covalent immobilization of B-*f*-MNPs on the surface of PG-*g*-GO via boroester bonds.

To study the weight loss patterns of the synthesized hybrid nanostructures, TGA curves of the samples were scrutinized and are shown in Fig. 5. As seen from Fig. 5a, TGA traces of pristine graphite shows a negligible weight loss, which is about 2% of its total weight in the entire temperature range. Comparing with the pristine graphite, GO shows much lower thermal stability. Although there is a weight loss about 2% below 100 °C due to the removal of physically adsorbed water, the major weight loss occurs at 180 °C. As shown in Fig. 5b, GO lose up to 98% of its total weight, which can be assigned to the pyrolysis of the labile oxygen-containing functional groups, yielding CO, CO_2 and steam [47]. On the other hand, the PG-*g*-GO and MNPs-*i*-PG-*g*-GO are more stable than GO as shown in Fig. 5c and d. For both the samples, the main weight loss occurred around 300–400 °C. The increased thermal stability of the hybrid nanostructures could be attributed to the chemical grafting

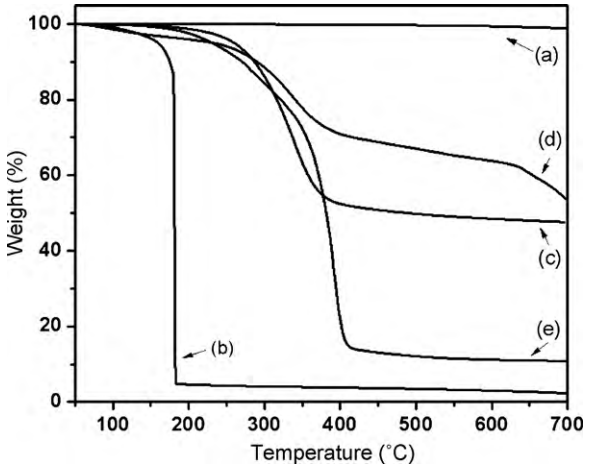

Fig. 5. TGA curves of (a) pristine graphite, (b) GO, (c) PG-*g*-GO, (d) MNPs-*i*-PG-*g*-GO and (e) pure PG.

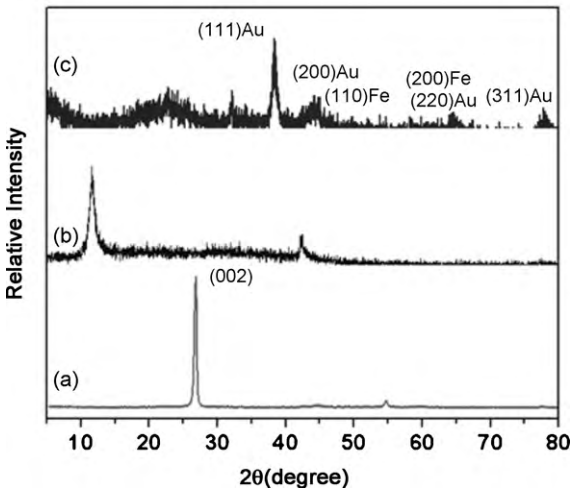

Fig. 6. XRD pattern of (a) pristine graphite, (b) GO and (c) MNPs-*i*-PG-*g*-GO.

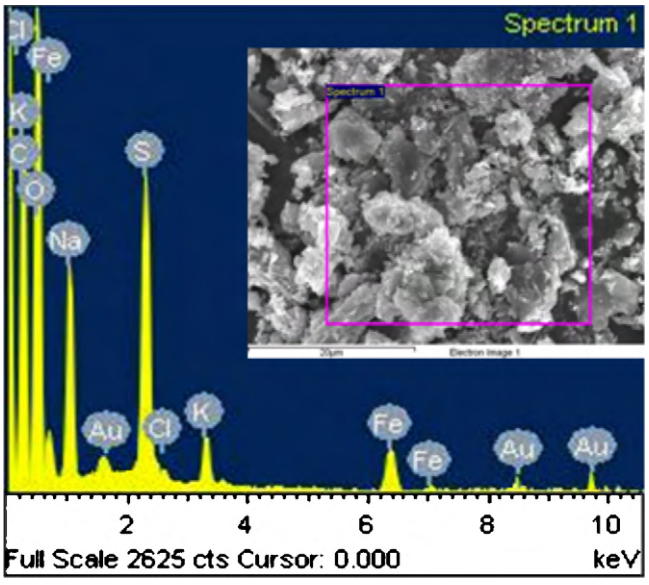

Fig. 7. EDX spectrum of MNPs-*i*-PG-*g*-GO.

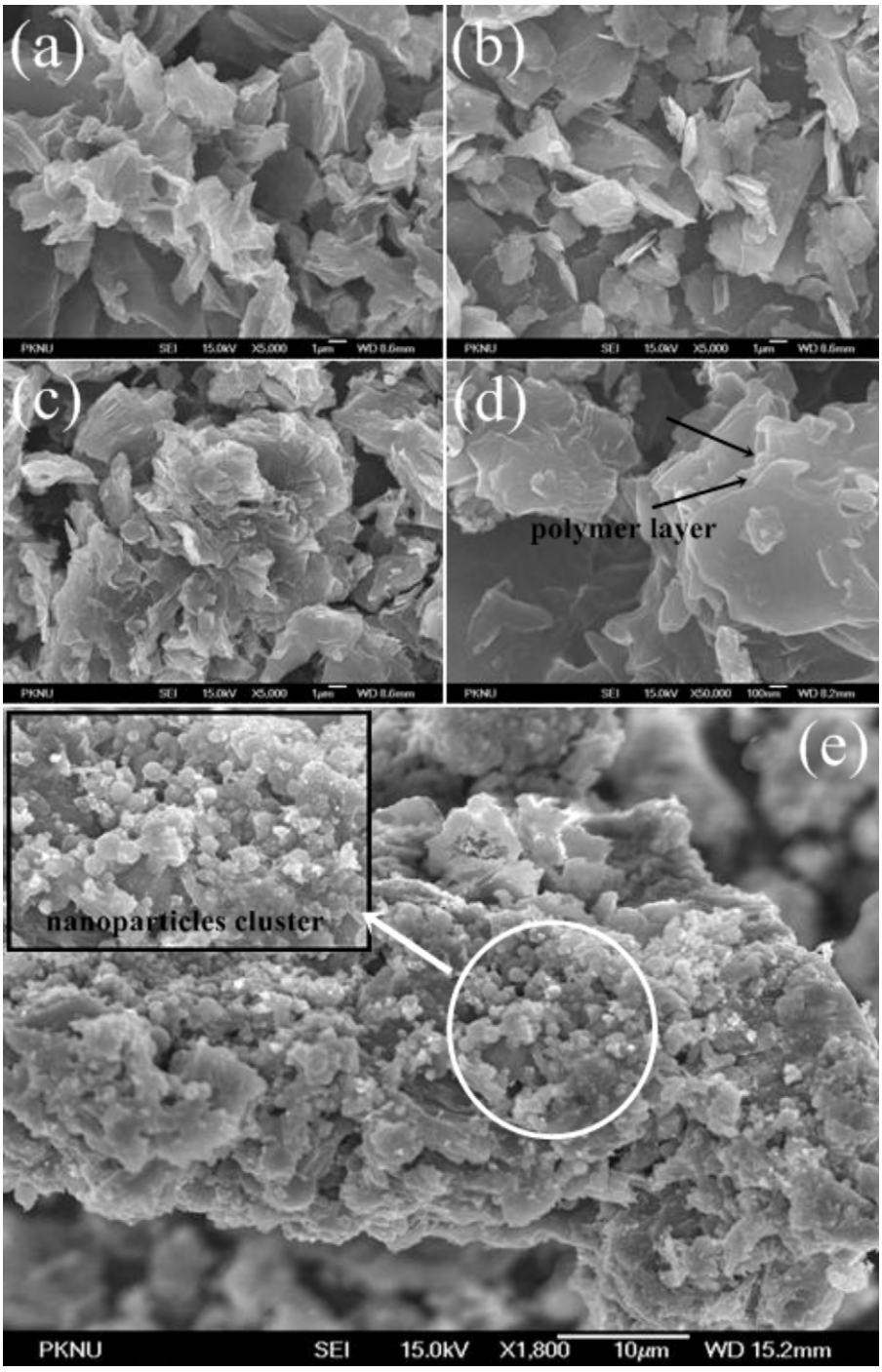

Fig. 8. FE-SEM images of (a) pristine graphite, (b) GO, (c, d) PG-*g*-GO and (e) MNPs-*i*-PG-*g*-GO.

of PG onto the GO surface. It is worthy to note that, in the case of MNPs-*i*-PG-*g*-GO hybrid nanostructure, besides the presence of PG via chemical grafting, the binding of B-*f*-MNPs on the PG-*g*-GO surface also contribute to the increase in their thermal stability. The decomposition curve of pure PG is given in Fig. 5e, which show a weight loss about 90% of its total weight which is in conjunction with previously reported study [48]. This also well suggests that the thermal stability of hybrid materials was better improved.

XRD measurements were employed to investigate the crystallinity of the synthesized hybrids. Fig. 6 depicts the XRD patterns of pristine graphite, GO and MNPs-*i*-PG-*g*-GO. While the characteristic peak corresponding to the (0 0 2) plane of pristine graphite appears at $2\theta = 26.67^\circ$, the GO pattern shows a strong peak at $2\theta = 11.7^\circ$, indicating the presence of oxygen-containing functional groups after the oxidation process as shown in Fig. 6b. The d-spacing of GO layers calculated as 0.43 nm is larger than that of the layers of pristine graphite (0.25 nm) [49]. As to the MNPs-*i*-PG-*g*-GO, after PG was grafted onto GO, the strong peak at 11.7° disappeared, indicating the PG was successfully grafted on the GO surface. In addition, the pattern of MNPs-*i*-PG-*g*-GO shows four additional weak diffraction peaks at $2\theta = 38.14^\circ$, 44.36°, 64.58° and 77.8°, which corresponds to the presence of Au and Fe nanoparticles on the surface of the samples (Fig. 6c). The results demonstrate that the Fe@Au

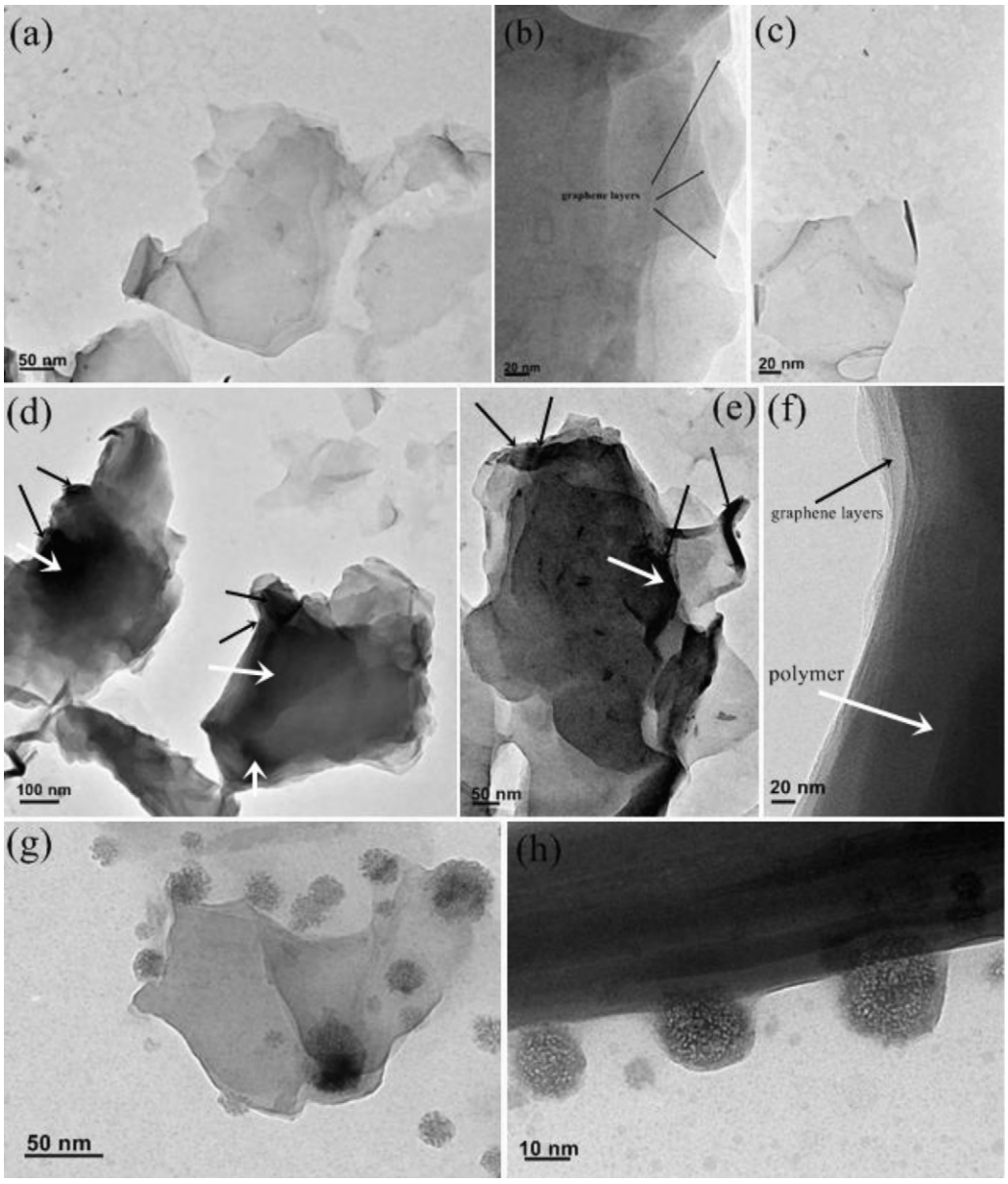

Fig. 9. HR-TEM images of (a–c) GO, of (d–f) PG-*g*-GO and of (g and h) MNPs-*i*-PG-*g*-GO at different magnifications.

nanoparticles were successfully immobilized onto the surface of PG-*g*-GO.

EDX analysis was also used to characterize the chemical composition of MNPs-*i*-PG-*g*-GO (Fig. 7). The spectrum clearly shows the presence of gold, iron, sulfur, carbon and oxygen elements in the sample, which further confirm successful preparation of the novel hybrid nanostructures.

3.3. Morphologies of hybrid nanostructures

The morphologies of pristine graphite and the hybrid nanostructures were studied using FE-SEM as shown in Fig. 8. Pristine graphite shows a laminated structure in which a large amount of sheets are stacked together (Fig. 8a). In the case of GO, because of oxidation process, the GO sheets break into pieces smaller than pristine graphite which was observed in Fig. 8b. On the other hand, as can be seen in Fig. 8c and d, the PG-*g*-GO sample clearly reveals the thickness increase of these sheets when compared to the layered structures of GO (marked by arrows). This morphological observation indicates the surface of GO was grafted with PG. The morphology of the MNP-*i*-PG-*g*-GO represented in Fig. 8e, clearly shows that the nanoparticle cluster was immobilized onto the PG-*g*-GO surface, hence indicating that there was strong interaction between PG-*g*-GO and B-*f*-MNPs via boroester bonds, which were formed between free hydroxyl functional groups present in PG and boronic acid.

In order to further investigate the morphologies of the prepared hybrids, HR-TEM images were recorded. Fig. 9 shows the TEM images of GO sheet, PG-*g*-GP and MNPs-*i*-PG-*g*-GO at different magnifications. From the TEM images of GO, it can be seen the presence of a mixture of graphene layers. In most cases, bilayer graphene and few layers graphene were observed (Fig. 9a). They are rippled and entangled with each other like a silk weave form (Fig. 9b and c). After the chemical grafting of PG onto the surface of GO, a significant change was observed. Fig. 9d shows morphology of PG-*g*-GO, in which the dark regions are related to the grafted PG onto the GO surface. It is interesting to note that the intensity of the dark color on the basal plane of GO is relatively higher than edges, indicating the higher density of grafted PG on these regions. It can be explained by higher density of hydroxyl functional groups

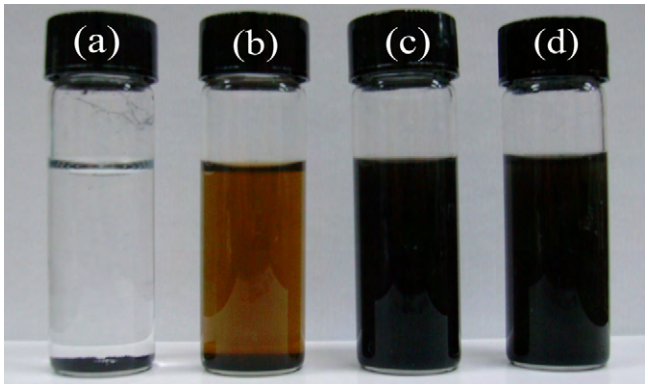

Fig. 10. Digital photographs of (a) pristine graphite, (b) GO, (c) PG-*g*-GO and (d) MNPs-*i*-PG-*g*-GO in distilled water.

on the basal plane of GO. At higher magnifications (Fig. 9e and f), arrows marked in the images indicate the thickness increase of GO sheet surface due to the coverage of the PG. Fig. 9g shows the morphology of MNP-*i*-PG-*g*-GO hybrid nanostructure. While most of the nanoparticles were immobilized onto the GO, and only few free nanoparticles were observed. It could be noticed that these nanoparticles are homogenously immobilized along with GO layers (Fig. 9h). It could be explained that the B-*f*-MNPs are immobilized to the PG-*g*-GO surface via the strong covalent bonding of boroester linkage, rather than being immobilized by simple physical absorption or hydrogen-bonding interaction.

3.4. Dispersion stability of hybrids in distilled water

To examine the dispersion stability of the hybrid nanostructures, all the samples were dispersed in distilled water at a typical concentration of 0.1 mg/mL followed by ultrasonication. The digital photographs provide a vivid observation on the water-dispersible property of the samples as shown in Fig. 10. The pristine graphite is not dispersible in water and tends to form sediments at the bottom of vial or float on top of water due to poor hydrogen-bonding (Fig. 10a). On the other hand, GO showed slightly better water-dispersible stability than pristine graphite, indicated by the yellow solution. Unlike pristine graphite, the presence of covalently attached oxygen-containing groups in GO surface such as hydroxyl and carboxyl groups renders it more hydrophilic. However, it is well-known that GO sheets, which have a high specific surface area, tend to form irreversible agglomerates to form graphite via strong π–π stacking and van der Waals interaction, indicating by the presence of solid at the bottom of vial as shown in Fig. 10b. In the case of PG-*g*-GO, after the grafting of the PG onto the surface of GO, the dispersibility of the hybrid nanostructure was dramatically increased due to the high hydrophilicity of PG. The homogeneous black color was obvious evidence for the perfect dispersibility in water of the PG-*g*-GO. The dispersed water solution was stable over 3 months without conspicuous aggregates (Fig. 10c). It is also interesting to note that after the immobilization of the B-*f*-MNPs to the PG-*g*-GO, the hybrid nanostructure still remained in well-dispersed state in water as seen in Fig. 10d.

4. Conclusions

In the present study, a facile strategy for the synthesis of water-dispersible graphene based on chemical grafting of PG onto the surface of GO nanosheets is developed. This is the first report on the covalent polymer functionalization of graphene through the facile approach based on *in situ* ring-opening polymerization of glycidol. Additionally, the Fe@Au nanoparticles were successfully functionalized using boronic acid through the well-developed Au–S chemistry. Considering a large number of free hydroxyl functional groups appending on the surface of PG-*g*-GO and B-*f*-MNPs, it is interesting to use prepared PG-*g*-GO as template for loading magnetic nanoparticles via boroester bonds. The synthesized novel hybrid nanostructures could be stably dispersed in water over 3 months and emerged as promising materials to meet various requirements for potential applications.

Acknowledgment

This research was financially supported by Corporate-affiliated Research Institute of Academic-Industrial-Institutional Cooperation Improvement Business. No. S7080008110.

References

[1] C.G. Navarro, M. Burghard, K. Kern, Nano Lett. 8 (2008) 2045.
[2] S. Park, K.S. Lee, G. Bozoklu, W. Cai, S.T. Nguyen, R.S. Ruoff, ACS Nano 3 (2008) 572.
[3] J. Wu, W. Pisula, K. Müllen, Chem. Rev. 107 (2007) 718.
[4] C.G. Navarro, R.T. Weitz, A.M. Bittner, M. Scolari, A. Mews, M. Burghard, K. Kern, Nano Lett. 7 (2007) 3499.
[5] A.A. Balandin, S. Ghosh, W. Bao, I. Calizo, D. Teweldebrhan, F. Miao, C.N. Lau, Nano Lett. 8 (2008) 902.
[6] J.M. Pereira, P. Vasilopoulos, F.M. Peeters, Nano Lett. 7 (2007) 946.
[7] K.S. Subrahamanyam, S.R.C. Vivekchand, A. Govindaraj, C.N.R. Rao, J. Mater. Chem. 18 (2008) 1517.
[8] H. Bai, C. Li, X. Wang, G. Shi, Chem. Commun. 46 (2010) 2376.
[9] J.R. Lomeda, C.D. Doyle, D.V. Kosynkin, W. Hwang, J.M. Tour, J. Am. Chem. Soc. 130 (2008) 16201.
[10] D. Konatham, A. Striolo, Nano Lett. 8 (2008) 4630.
[11] R. Kou, Y. Shao, D. Wang, M.H. Engelhard, J.H. Kwak, J. Wang, V.V. Viswanathan, C. Wang, Y. Lin, Y. Wang, I.A. Aksay, J. Liu, Electrochem. Commun. 11 (2009) 954.
[12] H. Zhang, X. Lv, Y. Li, Y. Wang, J. Li, ACS Nano 4 (2010) 380.
[13] J.D. Fowler, M.J. Allen, V.C. Tung, Y. Yang, R.B. Kaner, B.H. Weller, ACS Nano 3 (2009) 301.
[14] J.T. Robinson, F.K. Perkins, E.S. Snow, Z. Wei, P.E. Sheehan, Nano Lett. 8 (2008) 3137.
[15] P.K. Ang, W. Chen, A.T.S. Wee, K.P. Loh, J. Am. Chem. Soc. 130 (2008) 14392.
[16] F. Schedin, A.K. Geim, S.V. Morozov, E.W. Hill, P. Blake, M.I. Katsnelson, K.S. Novoselov, Nat. Mater. 6 (2007) 652.
[17] X. Wang, L. Zhi, K. Müllen, Nano Lett. 8 (2008) 323.
[18] V.Y. Aristov, G. Urbanik, K. Kummber, D.V. Vyalikh, O.V. Molodtsova, A.B. Preobrajenski, A.A. Zakharov, C. Hess, T. Hänke, B. Büchner, I. Vobornik, J. Fujii, G. Panaccione, Y.A. Ossipyan, M. Knupfer, Nano Lett. 10 (2010) 992.
[19] Z. Liu, Q. Liu, Y. Huang, Y. Ma, S. Yin, X. Zhang, W. Sun, Y. Chen, Adv. Mater. 20 (2008) 3924.
[20] Q. Liu, Z. Liu, X. Zhang, L. Yang, N. Zhang, G. Pan, S. Yin, Y. Chen, J. Wei, Adv. Funct. Mater. 19 (2009) 894.
[21] C. Di, D. Wei, G. Yu, Y. Liu, Y. Guo, D. Zhu, Adv. Mater. 20 (2008) 3289.
[22] N. Yang, J. Zhai, D. Wang, Y. Chen, L. Jiang, ACS Nano 4 (2010) 887.
[23] J. Yao, X. Shen, B. Wang, H. Liu, G. Wang, Electrochem. Commun. 11 (2009) 1849.
[24] G. Wang, X. Shen, J. Yao, J. Park, Carbon 47 (2009) 2049.
[25] X. Kang, J. Wang, H. Wu, I.A. Aksay, J. Liu, Y. Lin, Biosens. Bioelectron. 25 (2009) 901.
[26] N. Mohanty, V. Berry, Nano Lett. 8 (2008) 4469.
[27] C. Xu, X. Wang, Small 5 (2009) 2212.
[28] S. Niyogi, E. Bekyarova, M.E. Itkis, J.L. Mcwilliams, M.A. Hamon, R.C. Haddon, J. Am. Chem. Soc. 128 (2006) 7720.
[29] Y. Xu, H. Bai, G. Lu, C. Li, G. Shi, J. Am. Chem. Soc. 130 (2008) 5856.
[30] Q. Yang, X. Pan, F. Huang, K. Li, J. Phys. Chem. C 114 (2010) 3811.
[31] C. Zhu, S. Guo, Y. Fang, S. Dong, ACS Nano 4 (2010) 2429.
[32] H.J. Salavagione, M.A. Gómez, G. Martínez, Macromolecules 42 (2009) 6331.
[33] C. Shan, H. Yang, D. Han, Q. Zhang, A. Ivaska, L. Niu, Langmuir 25 (2009) 12030.
[34] R. Muszynski, B. Seger, P.V. Kamat, J. Phys. Chem. C 112 (2008) 5263.
[35] W. Hong, H. Bai, Y. Xu, Z. Yao, Z. Gu, G. Shi, J. Phys. Chem. C 114 (2010) 1822.
[36] F. Li, H. Yang, C. Shan, Q. Zhang, D. Han, A. Ivaska, L. Niu, J. Mater. Chem. 19 (2009) 4022.
[37] A.H. Lu, E.L. Salabas, F. Schüth, Angew. Chem. Int. Ed. 46 (2007) 1222.
[38] F.F. Fang, H.J. Choi, W.S. Choi, Colloid Polym. Sci. 288 (2010) 359.
[39] F.F. Fang, H.J. Choi, Y. Seo, ACS Appl. Mater. Interf. 2 (2010) 54.
[40] S.W. Ko, J.Y. Lim, B.J. Park, M.S. Yang, H.J. Choi, J. Appl. Phys. 105 (2009) 07E703.
[41] W. Hummers, R. Offerman, J. Am. Chem. Soc. 80 (1958) 1339.
[42] M. Adeli, N. Mirab, F. Zabihi, Nanotechnology 20 (2009) 485603.

[43] W.L. Zhou, E.E. Carpenter, J. Lin, A. Kumbhar, J. Sims, C.J. O'Connor, Eur. Phys. J. D 16 (2001) 289.
[44] S.J. Cho, J.C. Idrobo, J. Olamit, K. Liu, N.D. Browning, S.M. Kauzlarich, Chem. Mater. 17 (2005) 3181.
[45] A.L. Korich, K.M. Clarke, D. Wallace, P.M. Iovine, Macromolecules 42 (2009) 5906.
[46] T.A. Pham, S.M. Son, Y.T. Jeong, Synth. React. Inorg. Met.-Org. Chem. 40 (2010) 216.
[47] S. Stankovich, D.A. Dikin, R.D. Piner, K.A. Kohlhaas, A. Kleinhamma, Y. Jia, Y. Wu, S.T. Nguyen, R.S. Ruoff, Carbon 45 (2007) 1558.
[48] C. Siegers, M. Bielsalski, R. Haag, Chem. Eur. J. 10 (2004) 2831.
[49] M. Fang, K. Wang, H. Lu, Y. Yang, S. Nutt, J. Mater. Chem. 19 (2009) 7098.